Chinese Chemical Letters 35 (2024) 109191

Contents lists available at ScienceDirect

Chinese Chemical Letters

journal homepage: www.elsevier.com/locate/cclet

Multiple conductive network for $KTi_2(PO_4)_3$ anode based on MXene as a binder for high-performance potassium storage

Tong Su, Yue Wang, Qizhen Zhu*, Mengyao Xu, Ning Qiao*, Bin Xu*

State Key Laboratory of Organic-Inorganic Composites, Beijing Key Laboratory of Electrochemical Process and Technology for Materials, Beijing University of Chemical Technology, Beijing 100029, China

ARTICLE INFO

Article history:
Received 20 August 2023
Revised 15 September 2023
Accepted 6 October 2023
Available online 13 October 2023

Keywords:
MXene
$Ti_3C_2T_x$
$KTi_2(PO_4)_3$
Anode
Conductive network
Potassium storage

ABSTRACT

$KTi_2(PO_4)_3$ is a promising anode material for potassium storage, but suffers from low conductivity and difficult balance between high capacity and good structural stability. Herein, the $Ti_3C_2T_x$ MXene is used as a multifunctional binder to fabricate the $KTi_2(PO_4)_3$ electrode by the traditional homogenizing-coating method. The MXene nanosheets, together with the conductive agent super P nanoparticles, construct a multiple conductive network for fast electron/ion transfer and high electrochemical kinetics. Moreover, the network ensures the structural stability of the $KTi_2(PO_4)_3$ electrode during the de-intercalation/intercalation of 4 K^+ ions, which is beneficial for simultaneously achieving high capacity and good cycle performance. Therefore, the MXene-bonded $KTi_2(PO_4)_3$ electrode delivers a reversible capacity of 255.2 mAh/g at 50 mA/g, outstanding rate capability with 132.3 mAh/g at 2 A/g, and excellent cycle performance with 151.6 mAh/g at 1 A/g after 2000 cycles. This work not only suggests a high-performance anode material for potassium-ion batteries, but also demonstrates that the MXene is a promising binder material for constructing conductive electrodes in rechargeable batteries.

Lithium-ion batteries (LIBs) with high energy density have broad applications in electronic communication and electric vehicles [1–3], but the scarcity and uneven distribution of lithium resources sharply increase their cost and limit their application in large-scale energy storage system [4–6]. Potassium with similar physical and chemical properties to lithium attracts much attention because of its much more abundant reserves and lower cost [7,8]. Moreover, the redox potential of K/K^+ couple is −2.93 V *vs.* standard hydrogen electrode (SHE), indicating a high working voltage of potassium-ion batteries (PIBs). In addition, the potassium ion shows smaller Stokes radius (3.6 Å) in some organic solvents than the sodium ion (4.6 Å) and lithium ion (4.8 Å), implying high ionic conductivity of the potassium-based electrolyte [9,10]. Therefore, PIBs are considered as a promising alternative to LIBs in the field of large-scale energy storage [11]. Nevertheless, the electrode materials for PIBs usually suffer from large volume change during the de-intercalation/intercalation of the K^+ ions with large radius of 1.38 Å, leading to the structural instability and unsatisfactory cycle performance [12–14].

$KTi_2(PO_4)_3$ with high ionic conductivity and massive potassium storage sites has been explored as anode material for PIBs [15,16], but it shows low electronic conductivity and difficult balance between high capacity and good structural stability. Han *et al.* [17] firstly reported a carbon-coated $KTi_2(PO_4)_3$ anode material, which delivered only a small capacity of 72.6 mAh/g in a potential range of 1.2–2.8 V (*vs.* K/K^+). Later, Du *et al.* [18] improved the capacity of $KTi_2(PO_4)_3$@C nanocomposite to 292.7 mAh/g by expanding the potential range to 0.01–3 V (*vs.* K/K^+), corresponding to the de-intercalation/intercalation of 4 K^+ during charging-discharging, which caused large volume change and sacrificed the cycle performance to some extent. To guarantee the cycle stability, Voronina *et al.* [19] prepared a carbon-modified $KTi_2(PO_4)_3$ and carried out the electrochemical test in 1–4.0 V (*vs.* K/K^+) for only 2 K^+ de-intercalation/intercalation at ~1.6 V, which displayed a capacity of 126 mAh/g and good cycle stability with 89% capacity retention after 500 cycles. Nowadays, the development of $KTi_2(PO_4)_3$ for potassium storage is still in the early stage, and the simultaneous achievement of high capacity, high conductivity and good structural stability during cycling is still a challenge for the $KTi_2(PO_4)_3$ anode.

Two-dimensional (2D) transition metal carbides/nitrides, known as MXenes with a general formula of $M_{n+1}X_nT_x$, where M expresses the early transition metals like Ti, V, Nb, Mo, *etc.*, X is

* Corresponding authors.
E-mail addresses: zhuqz@mail.buct.edu.cn (Q. Zhu), qiaoning@buct.edu.cn (N. Qiao), xubin@mail.buct.edu.cn (B. Xu).

https://doi.org/10.1016/j.cclet.2023.109191
1001-8417/

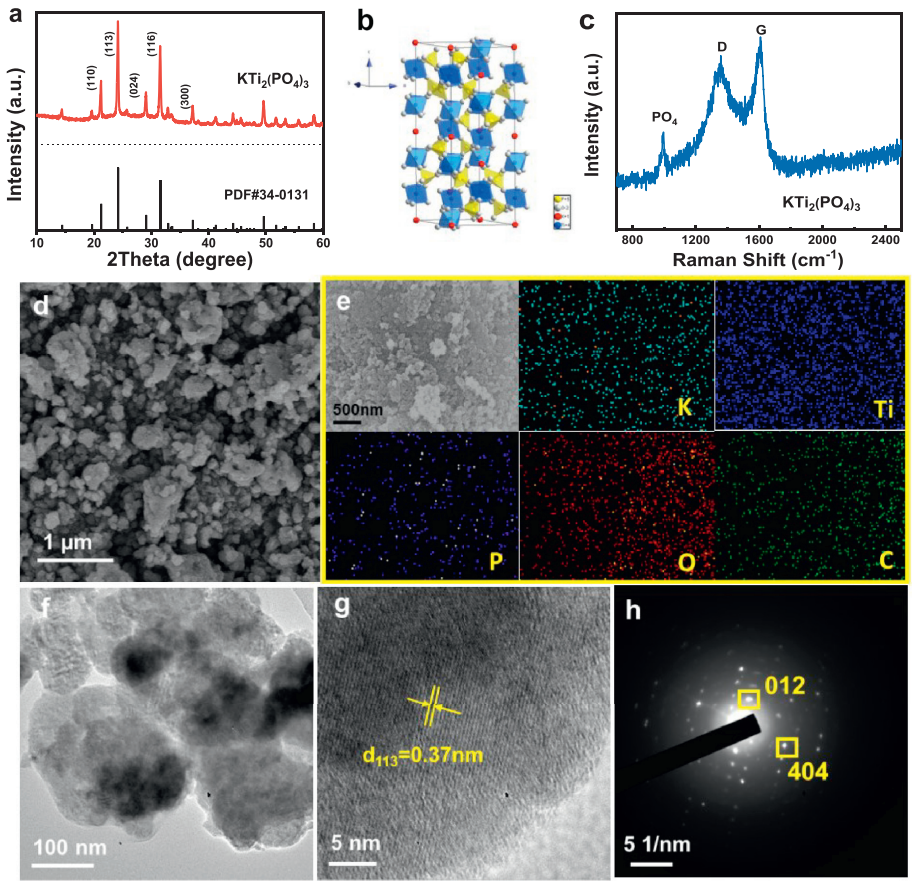

Fig. 1. Structure and composition of the prepared $KTi_2(PO_4)_3$. (a) XRD pattern. (b) Crystal structure. (c) Raman spectrum. (d) SEM image. (e) Elemental mapping images of K, Ti, P, O and C. (f) TEM image. (g) HRTEM image with (h) the corresponding SAED pattern.

C and/or N, and T_x represents the terminations such as –F, –OH and –O [20–23], gain great attention in energy storage field owing to their 2D lamella structure, large surface area, metallic-like electronic conductivity, high mechanical strength and good dispersibility in aqueous and some organic solutions [24–26]. Our previous works have confirmed that the MXene nanosheets can be used as a conductive binder for film electrode fabrication through the vacuum-filtration method [27–30]. Here, we further propose the assembly of the $KTi_2(PO_4)_3$ electrode with MXene as a multifunctional binder through the conventional homogenizing-coating strategy, in which the highly conductive MXene sheets, together with the super P (SP) nanoparticles, construct a multiple conductive network for fast charge transfer, remarkably enhancing the utilization of the active material $KTi_2(PO_4)_3$ and improving the rate capability of the anode. Moreover, the lamella structure and good mechanical strength of the MXene are beneficial for protecting the electrode structural stability, endowing the $KTi_2(PO_4)_3$ anode with superior cycle performance.

The $KTi_2(PO_4)_3$ nanoparticles were prepared by a solvothermal process followed by thermal treatment at 750 °C under N_2 atmosphere (Fig. S1 in Supporting information). XRD pattern of the as-prepared $KTi_2(PO_4)_3$ (Fig. 1a) shows the diffraction peaks in good agreement with the rhombohedral $KTi_2(PO_4)_3$ phase (PDF#34-0131), indicating its high crystallinity. Accordingly, the NASICON structure of $KTi_2(PO_4)_3$ is described in Fig. 1b, in which the TiO_6 octahedron and PO_4 tetrahedron are connected at the same point to construct a 3D framework with large interstitial spaces for fast K^+ ion transport. As the used organic raw materials (*e.g.*, CH_3COOK and $C_{16}H_{36}O_4Ti$) inevitably introduce carbon in the preparation procedure, the carbon content of the prepared $KTi_2(PO_4)_3$ sample is tested to be ~1.51% by TG curve from room temperature to 600 °C in Fig. S2 (Supporting information). Furthermore, the $KTi_2(PO_4)_3$ sample exhibits two Raman peaks at 1355 cm^{-1} and 1595 cm^{-1} (Fig. 1c), corresponding to the D peak (disordered carbon or defective graphitic band) and G peak (crystalline graphite band), respectively. The area ratio of D peak and G peak is calculated to be 2.754, meaning the carbon in the prepared sample is amorphous. In addition, there is a peak at 985 cm^{-1}, representing the stretching vibration of P-O bond in PO_4 tetrahedral of the $KTi_2(PO_4)_3$ bulk phase. As observed in SEM image in Fig. 1d, the $KTi_2(PO_4)_3$ sample shows irregular particles in nanoscale size, and the EDS mapping (Fig. 1e) displays the homogeneous distributions of the K, Ti, P, O and C elements that accords with the $KTi_2(PO_4)_3$ molecule structure (Table S1 in Supporting information). The TEM image further reveals that the $KTi_2(PO_4)_3$ particle sizes are in a range of 150–200 nm (Fig. 1f). Moreover, the lattice fringes of 0.37 nm corresponding to (113) crystal plane (Fig. 1g), and the diffraction rings signing (012) and (404) planes of $KTi_2(PO_4)_3$ (Fig. 1h) are exhibited.

Since the high capacity of $KTi_2(PO_4)_3$ requires the expanded potential range of 0.01–3 V (*vs.* K/K^+) for 4 K^+ de-intercalation/intercalation, from the view of electrode assembly, 2D MXene nanosheets are employed to construct a conductive framework to promote fast charge transport and limit the structure change, promising the achievement of both good cycle stability and high capacity. The $KTi_2(PO_4)_3$ electrode is prepared by the traditional homogenizing-coating process with SP as a conductive agent and $Ti_3C_2T_x$ MXenes as a conductive binder instead of conventional polymer binder, and the electrode is denoted as MXene-KTP (Fig. S3 in Supporting information). The $KTi_2(PO_4)_3$ electrodes with

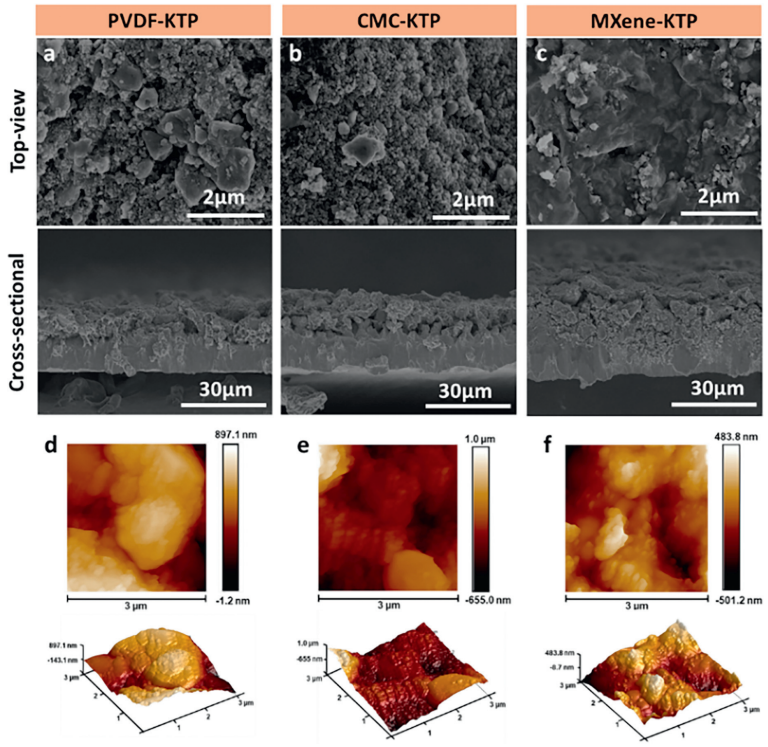

Fig. 2. Morphologies of the $KTi_2(PO_4)_3$ electrodes with PVDF, CMC or MXene as a binder. Top-view and cross-sectional SEM images of (a) PVDF-KTP, (b) CMC-KTP and (c) MXene-KTP. AFM images of (d) PVDF-KTP, (e) CMC-KTP, and (f) MXene-KTP.

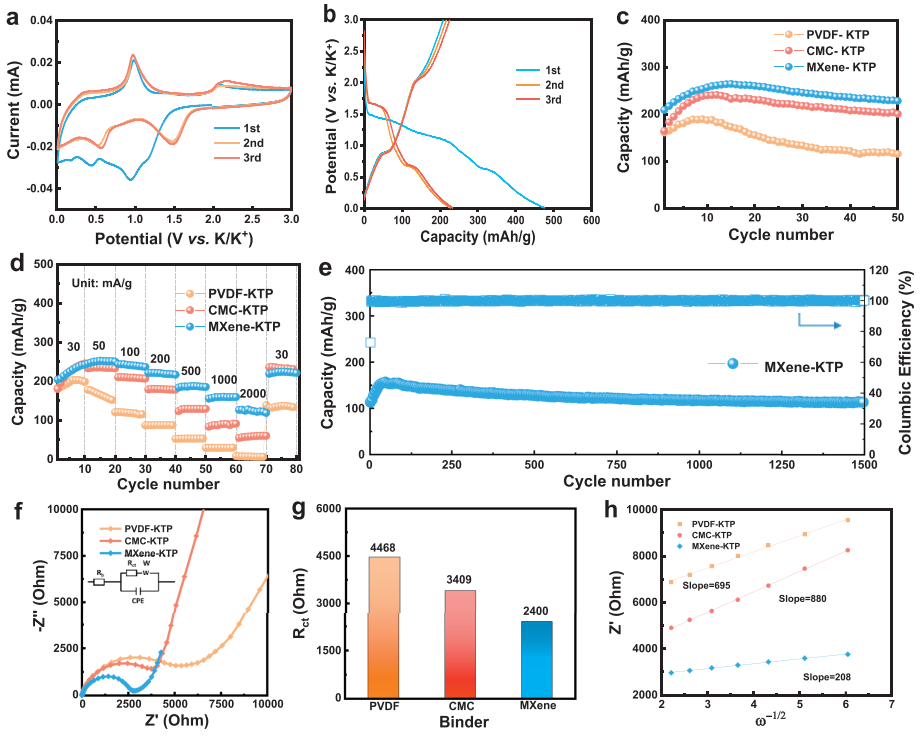

Fig. 3. Electrochemical performance of MXene-KTP for potassium storage. (a) CV curves at a scan rate of 0.1 mV/s. (b) Charge/discharge profiles at 50 mA/g. (c) Cycle performance at 50 mA/g. (d) Rate capability. (e) Long-term cycle stability at 1 A/g. (f) EIS spectra with the equivalent circuit in the inset. (g) R_{ct} values fitting by the equivalent circuit. (h) Relationship between Z' and square root of frequency $\omega^{-1/2}$ in the low-frequency region of the EIS spectra.

polyvinylidene difluoride binder (PVDF-KTP) and carboxymethylcellulose sodium binder (CMC-KTP) are also prepared *via* the similar process for comparison.

XRD pattern of the constructed MXene-KTP electrode reveals the characteristic peak at 6.2° corresponding to (002) plane of $Ti_3C_2T_x$ MXene, indicating the existence of MXene nanosheets (Fig. S4 in Supporting information). The surface morphologies and cross-sectional microstructures of the $KTi_2(PO_4)_3$ electrodes with PVDF, CMC and $Ti_3C_2T_x$ MXene binder are shown in Figs. 2a–c. The three electrodes are all composed of evenly dispersed $KTi_2(PO_4)_3$

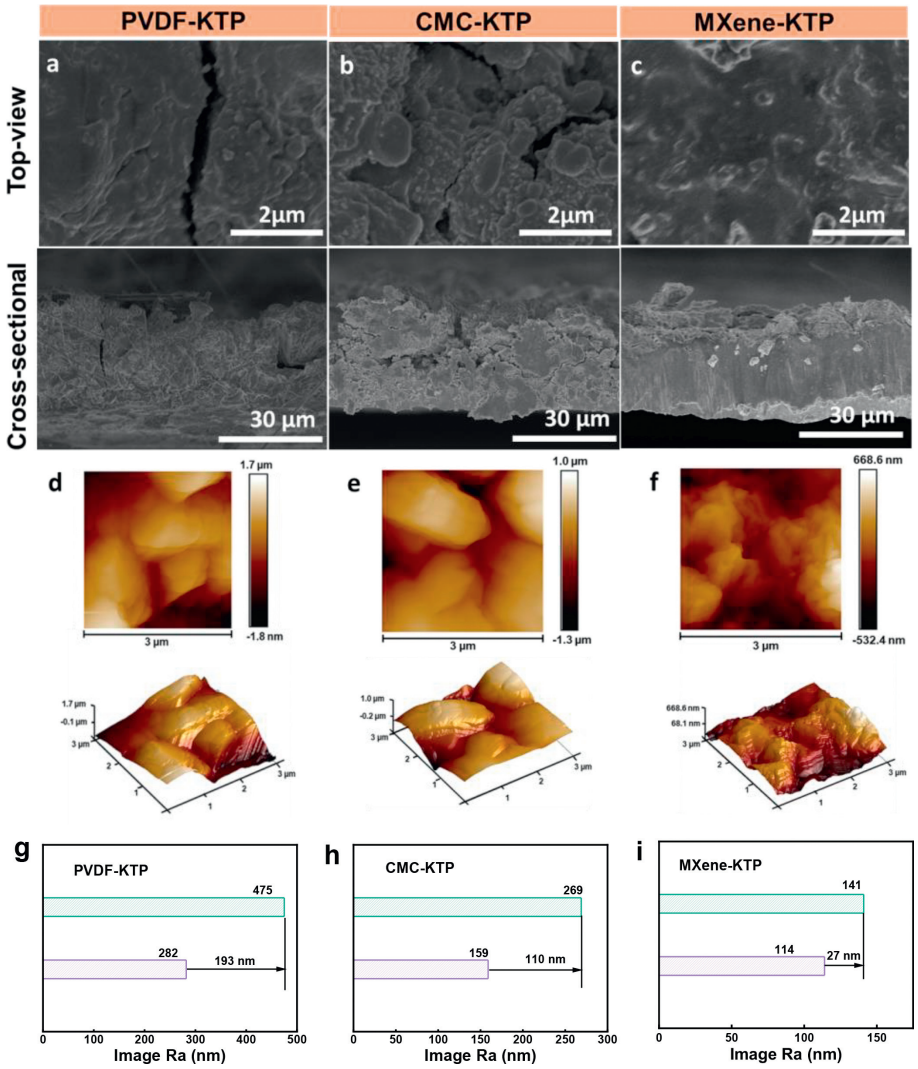

Fig. 4. Morphologies of the cycled $KTi_2(PO_4)_3$ electrodes. Top-view and cross-sectional SEM images of (a) PVDF-KTP, (b) CMC-KTP and (c) MXene-KTP; AFM images of (d) PVDF-KTP, (e) CMC-KTP, and (f) MXene-KTP; Roughness difference of (g) PVDF-KTP, (h) CMC-KTP and (i) MXene-KTP.

and SP nanoparticles, among which the MXene-KTP possesses the flattest surface with the $KTi_2(PO_4)_3$ particles evenly embedded in the conductive framework constructed by the SP nanoparticles and the MXene nanosheets. The digital photo of the MXene-KTP electrode shows the smooth surface and good wettability with 3 mol/L KFSI in DME electrolyte (Fig. S5 in Supporting information). Furthermore, the roughnesses of PVDF-KTP, CMC-KTP and MXene-KTP are 282, 159 and 114 nm, respectively (Figs. 2d–f), verifying the smoothness and the uniformity of the MXene-KTP electrode, which is beneficial for enhancing the structural stability and ensuring the rapid charge transfer in the electrode. The electronic conductivities of the electrodes confirm the superiority of the MXene-KTP, which displays a much higher conductivity of 45.6 S/cm compared to the PVDF-KTP (0.185 S/cm) and CMC-KTP (0.228 S/cm) electrodes (Fig. S6 in Supporting information).

The CV curves of the PVDF-KTP, CMC-KTP and MXene-KTP electrodes (Fig. 3a and Fig. S7 in Supporting information) at 0.1 mV/s in 0.01–3.0 V (*vs.* K/K^+) have two pairs of redox peaks at 1.60 V (red.)/2.10 V (ox.) and 0.65 V (red.)/0.91 V (ox.), corresponding to the redox reaction of Ti^{4+}/Ti^{3+} and Ti^{3+}/Ti^{2+} pairs, respectively [31,32]. The irreversible reduction peaks in the first cycle that disappear in the following cycles are attributed to the electrolyte decomposition and the formation of SEI film [33,34]. Also, the charge/discharge profiles of the three $KTi_2(PO_4)_3$ electrodes in Fig. 3b and Fig. S8 (Supporting information) show the electrochemical behavior in agreement with the CV curves.

The initial reversible potassium storge capacities of the PVDF-KTP, CMC-KTP, MXene-KTP electrodes are 160.9, 164.7 and 208.9 mAh/g at 50 mA/g, respectively (Fig. 3c). Due to the activation process, the capacities of the electrodes gradually increase in the initial cycles. However, the PVDF-KTP suffers from rapid capacity decay with only 115.5 mAh/g after 50 cycles, while the CMC-KTP electrode also has unsatisfactory cycle stability with 200.4 mAh/g after 50 cycles. By contrast, the MXene-KTP electrode delivers superior cycle performance, which exhibits a capacity of 228.3 mAh/g after 50 cycles. The enhancement of capacity and cycle performance is ascribed to the 2D MXene binder that can both facilitate electron transfer and buffer the volume change of the $KTi_2(PO_4)_3$ particles. The rate performance further highlights the superiority of MXene-KTP, which shows the capacities of 221.5, 184.2, 155.8 mAh/g at 200, 500, 1000 mA/g, respectively (Fig. 3d). Even at the high current density of 2 A/g, the capacity can still maintain at 126.9 mAh/g, much higher than that of PVDF-KTP (7.8 mAh/g) and CMC-KTP (55.0 mAh/g) electrodes. Fig. 3e reveals the long-term cycle performance of the MXene-KTP electrode, which possesses an initial capacity of 113.2 mAh/g at 1 A/g that increases to 156.8

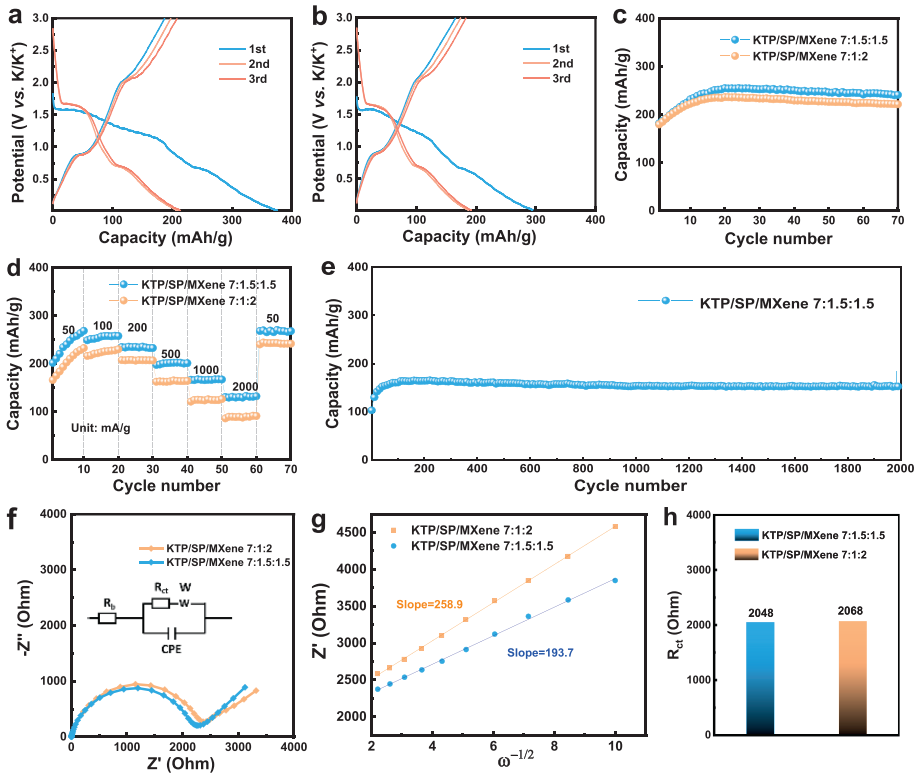

Fig. 5. Potassium storage performance of the $KTi_2(PO_4)_3$ electrode prepared with different ratios of SP and MXene. Charge/discharge curves of (a) KTP/SP/MXene 7:1.5:1.5 and (b) KTP/SP/MXene 7:1:2 at 50 mA/g. (c) Cycle performance at 50 mA/g. (d) Rate performance. (e) Long-term cycle stability at 1 A/g. (f) EIS spectra with the equivalent circuit in the inset. (g) Relationship between Z' and square root of frequency $\omega^{-1/2}$ in the low-frequency region of the EIS spectra. (h) R_{ct} values fitting by the equivalent circuit.

mAh/g after the activation process, and remains at 114.3 mAh/g after 1500 cycles. The outstanding cycle and rate performance is attributed to its excellent conductivity and structural stability originated from the 2D MXene nanosheets with metallic-like electronic conductivity and high mechanical strength as a conductive binder.

To study the kinetics of the electrodes, their EIS spectra are shown in Fig. 3f. Fitted with the equivalent circuit, the charge-transfer resistance (R_{ct}) of the MXene-KTP is calculated to be 2400 Ω, lower than that of PVDF-KTP and CMC-KTP (Fig. 3g). Moreover, the potassium-ion diffusion coefficients are calculated according to the slope of the plots of Z_{re} *versus* $\omega^{-1/2}$ in the low-frequency region (Fig. 3h) [35]. The potassium-ion diffusion coefficient of MXene-KTP (1.1×10^{-11} cm^2/s) are much higher than that of CMC-KTP (9.6×10^{-13} cm^2/s) and PVDF-KTP (6.0×10^{-13} cm^2/s), demonstrating accelerated potassium-ion transport. It means the conductive network constructed by the MXene binder not only effectively promotes the electron transfer, but also provides high porosity (Fig. S9 in Supporting information) for fast ion diffusion in the electrode, which is of great importance for achieving good rate performance.

To investigate the effect of the binder on the electrode structural stability, the morphologies of the $KTi_2(PO_4)_3$ electrodes using different binders after 100 cycles are compared. It can be seen that the big crevices appear on the surface and inside of the PVDF-KTP (Fig. 4a) and CMC-KTP (Fig. 4b) electrodes, which may cause the material pulverization and exfoliation from the current collector during cycling, leading to rapid capacity decay. Nevertheless, the cycled MXene-KTP electrode retains an intact surface without obvious crack and pulverization phenomenon (Fig. 4c). Furthermore, the surface roughnesses of the cycled PVDF-KTP, CMC-KTP and MXene-KTP electrodes are 475, 269 and 141 nm, respectively (Figs. 4d–f). As shown in Figs. 4g–i, the roughness difference of the MXene-KTP before and after cycling (27 nm) is much smaller than that of PVDF-KTP (193 nm) and CMC-KTP (110 nm), indicating that the MXene used as a binder can significantly improve the structural stability of the $KTi_2(PO_4)_3$ electrode, as well as fully contact with the active $KTi_2(PO_4)_3$ particles and promote fast electron transfer.

The 2D MXene nanosheets with metallic-like electronic conductivity, as above confirmed, significantly improve the electrochemical performance of the $KTi_2(PO_4)_3$ electrode when used as a binder. In the MXene-KTP electrode, the SP nanoparticles and the MXene nanosheets construct a multiple conductive framework. Therefore, the ratio of SP and MXene is important for the electrode to achieve both fast electron transfer and rapid ion transport. To optimize the electrode structure and performance, in addition to the above-mentioned MXene-KTP (KTP:SP:MXene = 7:2:1 in mass), two electrodes with different ratios of KTP:SP:MXene (7:1.5:1.5 and 7:1:2 in mass) are also prepared. With the MXene content increasing, the surface of the electrode is gradually covered (Fig. S10 in Supporting information), which may protect the electrode structure but cause the hindrance of the ion transport. As shown in Figs. 5a and b, the two electrodes show similar electrochemical behavior to the MXene-KTP with two plateaus at ~1.7 V and ~0.7 V during discharge process, corresponding to the redox reaction of Ti^{4+}/Ti^{3+} and Ti^{3+}/Ti^{2+} pairs, respectively.

Among the three electrodes with different SP and MXene ratios, the KTP/SP/MXene 7:1.5:1.5 delivers the highest reversible capacity of 255.2 mAh/g at 50 mA/g after activation and exhibits the best cycle performance with a capacity of 241.2 mAh/g after 70 cycles (Fig. 5c). Beside, it maintains structural integrality and stability after cycling (Fig. S11 in Supporting information). As exhibited in Fig. 5d and Fig. S12 (Supporting information), the KTP/SP/MXene 7:1.5:1.5 possesses excellent rate performance with capacities of

167.2 and 132.3 mAh/g at current densities of 1 and 2 A/g, respectively, demonstrating the optimized multiple conductive network with the cooperation of 2D MXene nanosheets and SP nanoparticles. In the conductive network, the MXene nanosheets can realize the rapid electron transfer on the plane, while the SP particles can provide the "point-to-point" electron transfer, which endows the active particles outside the MXene layers with high electron conduction. As the excess MXene may suffer from the sheet stacking that hinders the ion transport, while too low MXene content is not enough for constructing the highly conductive framework, to maximize the performance of the $KTi_2(PO_4)_3$ electrode, the appropriate proportion of SP and MXene is optimized to be 1.5:1.5.

As expected, the KTP/SP/MXene 7:1.5:1.5 electrode displays superior long-term cycle stability at a high current density of 1 A/g (Fig. 5e). It shows an initial reversible capacity of 103.2 mAh/g that gradually increases to 161.1 mAh/g due to the activation process, and maintains at 151.6 mAh/g after 2000 cycles, corresponding to a capacity retention of ~94.1% (compared with the maximum capacity after activation), which is attractive among the potassium storage anode materials when compared with the previously reported literatures (Table S2 in Supporting information). Based on the EIS plots (Fig. 5f), the potassium-ion diffusion coefficient of KTP/SP/MXene 7:1.5:1.5 is calculated to be 1.2×10^{-11} cm^2/s (Fig. 5g), and its R_{ct} value is 2048 Ω (Fig. 5h). It means the KTP/SP/MXene 7:1.5:1.5 has the best charge transfer capability among the MXene-boned $KTi_2(PO_4)_3$ electrodes, as its appropriate proportion can maximize the function of the MXene in constructing the highly conductive framework for both fast electron transfer and rapid ion transport, and meanwhile realize the "point-to-point" electron transfer of SP particles.

It is interesting that the KTP/SP/MXene 7:1.5:1.5 electrode can also be used for lithium storage. As shown in Figs. S13 and S14 (Supporting information), its lithium storage behavior is different from the potassium storage, which has broad CV peaks and slope charge/discharge profiles, implying the pseudocapacitive contribution. Furthermore, the lithium storage performance of the KTP/SP/MXene 7:1.5:1.5 electrode is very attractive with an initial reversible capacity of 471.3 mAh/g at 100 mA/g and a coulombic efficiency of 61.48%. It also achieves excellent cycle performance with a capacity retention of 93.5% after 50 cycles (Fig. S15 in Supporting information). Even at an ultrahigh current density of 10 A/g, it still displays a capacity of 102.8 mAh/g (Fig. S16 in Supporting information). Additionally, it shows a capacity of 300.2 mAh/g after 200 cycles at 1 A/g (Fig. S17 in Supporting information), demonstrating its promising potential as anode material for LIBs.

In conclusion, the $KTi_2(PO_4)_3$ electrode with MXene as a binder was prepared by homogenizing-coating method for PIBs, in which the 2D MXene nanosheets, together with the conductive agent SP nanoparticles, construct a multiple conductive network for the active $KTi_2(PO_4)_3$ particles. In the multiple conductive network, the MXene nanosheets facilitate rapid electron transfer on the plane and the SP nanoparticles endow with the "point-to-point" electron conduction. It also endows the electrode with fast ion diffusion and ensures the electrode structural stability during charge/discharge cycling, leading to the simultaneous achievement of high capacity, fast redox kinetics and good cycle performance. The KTP/SP/MXene 7:1.5:1.5 electrode displays a capacity of 255.2 mAh/g at 50 mA/g, superior rate performance (132.3 mAh/g at 2 A/g) and excellent long-term cycle stability with 151.6 mAh/g at 1 A/g after 2000 cycles. This work not only provides a promising candidate anode material for high-performance PIBs, but also propose a strategy with MXene as a binder to construct multiple conductive network for fabricating electrode with active materials with low conductivity and unsatisfactory structural stability.

Declaration of competing interest

The authors declare no conflict of interest.

Acknowledgment

The authors acknowledge the financial support by National Natural Science Foundation of China (No. U2004212).

Supplementary materials

Supplementary material associated with this article can be found, in the online version, at doi:10.1016/j.cclet.2023.109191.

References

[1] J. Xiang, Y. Wei, Y. Zhong, et al., Adv. Mater. 34 (2022) 2200912.
[2] J. Liu, H. Shi, K. Yu, et al., Chin. Chem. Lett. 34 (2023) 108274.
[3] X. Min, J. Xiao, M. Fang, et al., Energy Environ. Sci. 14 (2021) 2186–2243.
[4] X. Jiang, Y. Chen, X. Meng, et al., Carbon 191 (2022) 448–470.
[5] T. Wang, J. Sha, W. Wang, et al., Chin. Chem. Lett. 34 (2023) 107929.
[6] J. Mao, C. Ye, S. Zhang, et al., Energy Environ. Sci. 15 (2022) 2732–2752.
[7] Z.X. Huang, Z.Y. Gu, Y.L. Heng, et al., Chem. Eng. J. 452 (2023) 139438.
[8] T. Hosaka, K. Kubota, A.S. Hameed, et al., Chem. Rev. 120 (2020) 6358–6466.
[9] V. Gabaudan, L. Monconduit, L. Stievano, et al., Front. Energy Res. 7 (2019) 46.
[10] K. Kubota, M. Dahbi, T. Hosaka, et al., Chem. Rec. 18 (2018) 459–479.
[11] X. Chang, Q. Zhu, Q. Zhao, et al., ACS Appl. Mater. Interfaces 15 (2023) 7999–8009.
[12] X. Chang, N. Sun, H. Zhou, et al., Chin. Chem. Lett. 34 (2023) 107312.
[13] Y. Xia, W. Jin, Y. Qi, et al., Chin. Chem. Lett. 32 (2021) 2433–2437.
[14] P. Zhang, Y. Peng, Q. Zhu, et al., Energy Environ. Mater. (2022), doi:10.1002/eem2.12379.
[15] S. Chen, C. Wu, L. Shen, et al., Adv. Mater. 29 (2017) 1700431.
[16] Z. Jian, Y.S. Hu, X. Ji, et al., Adv. Mater. 29 (2017) 1601925.
[17] J. Han, Y. Niu, S.J. Bao, et al., Chem. Commun. 52 (2016) 11661–11664.
[18] Z. Wei, D. Wang, M. Li, et al., Adv. Energy Mater. 8 (2018) 1801102.
[19] N. Voronina, J.H. Jo, A. Konarov, et al., Small 16 (2020) 2001090.
[20] M. Naguib, M. Kurtoglu, V. Presser, et al., Adv. Mater. 23 (2011) 4248–4253.
[21] X. Zhang, J. Miao, P. Zhang, et al., Chin. Chem. Lett. 31 (2020) 2305–2308.
[22] L. Fu, W. Xia, Adv. Eng. Mater. 23 (2021) 2001191.
[23] Y. Li, Q. Zhu, M. Xu, et al., Adv. Funct. Mater. 33 (2023) 2213416.
[24] Y. Wei, P. Zhang, R.A. Soomro, et al., Adv. Mater. 33 (2021) 2103148.
[25] P. Zhang, R.A. Soomro, Z. Guan, et al., Energy Storage Mater. 29 (2020) 163–171.
[26] P. Liu, P. Xiao, M. Lu, et al., Chin. Chem. Lett. 34 (2023) 107426.
[27] N. Sun, Q. Zhu, B. Anasori, et al., Adv. Funct. Mater. 29 (2019) 1906282.
[28] L. Yu, L. Hu, B. Anasori, et al., ACS Energy Lett. 3 (2018) 1597–1603.
[29] P. Zhang, Q. Zhu, Z. Guan, et al., ChemSusChem 13 (2019) 1621–1628.
[30] Q. Zhao, Q. Zhu, J. Miao, et al., Small 15 (2019) 1904293.
[31] P. Senguttuvan, G. Rousse, M.E. Arroyoy de Dompablo, et al., J. Am. Chem. Soc. 135 (2013) 3897–3903.
[32] G. Yang, H. Song, M. Wu, et al., J. Mater. Chem. A 3 (2015) 18718–18726.
[33] Y. Dong, Z.S. Wu, S. Zheng, et al., ACS Nano 11 (2017) 4792–4800.
[34] W. Zhang, J. Mao, S. Li, et al., J. Am. Chem. Soc. 139 (2017) 3316–3319.
[35] H. Song, M. Luo, A. Wang, ACS Appl. Mater. Interfaces 9 (2017) 2875–2882.